The low-mass content of the massive young star cluster RCW 38

Koraljka Mužić,[1,2]* Rainer Schödel,[3] Alexander Scholz,[4] Vincent C. Geers,[5] Ray Jayawardhana,[6] Joana Ascenso[7,8] and Lucas A. Cieza[1]

[1]*Núcleo de Astronomía, Facultad de Ingeniería, Universidad Diego Portales, Av. Ejercito 441, Santiago, Chile*
[2]*SIM/CENTRA, Faculdade de Ciencias de Universidade de Lisboa, Ed. C8, Campo Grande, P-1749-016 Lisboa, Portugal*
[3]*Instituto de Astrofísica de Andalucía (CSIC), Glorieta de la Astronomá s/n, E-18008 Granada, Spain*
[4]*SUPA, School of Physics & Astronomy, St. Andrews University, North Haugh, St Andrews KY16 9SS, UK*
[5]*UK Astronomy Technology Centre, Royal Observatory Edinburgh, Blackford Hill, Edinburgh EH9 3HJ, UK*
[6]*Faculty of Science, York University, 355 Lumbers Building, 4700 Keele Street, Toronto, ON M3J 1P2, Canada*
[7]*CENTRA, Instituto Superior Tecnico, Universidade de Lisboa, Av. Rovisco Pais 1, P-1049-001 Lisbon, Portugal*
[8]*Departamento de Engenharia Física da Faculdade de Engenharia, Universidade do Porto, Rua Dr. Roberto Frias, s/n, P-4200-465 Porto, Portugal*

ABSTRACT

RCW 38 is a deeply embedded young ($\sim$1 Myr), massive star cluster located at a distance of 1.7 kpc. Twice as dense as the Orion nebula cluster, orders of magnitude denser than other nearby star-forming regions and rich in massive stars, RCW 38 is an ideal place to look for potential differences in brown dwarf formation efficiency as a function of environment. We present deep, high-resolution adaptive optics data of the central $\sim$0.5 $\times$ 0.5 pc^2 obtained with NACO at the Very Large Telescope. Through comparison with evolutionary models, we determine masses and extinction for $\sim$480 candidate members, and derive the first initial mass function (IMF) of the cluster extending into the substellar regime. Representing the IMF as a set of power laws in the form $dN/dM \propto M^{-\alpha}$, we derive the slope $\alpha = 1.60 \pm 0.13$ for the mass range 0.5–20 M$_\odot$, which is shallower than the Salpeter slope, but in agreement with results in several other young massive clusters. At the low-mass side, we find $\alpha = 0.71 \pm 0.11$ for masses between 0.02 and 0.5 M$_\odot$, or $\alpha = 0.81 \pm 0.08$ for masses between 0.02 and 1 M$_\odot$. Our result is in agreement with the values found in other young star-forming regions, revealing no evidence that a combination of high stellar densities and the presence of numerous massive stars affects the formation efficiency of brown dwarfs and very-low-mass stars. We estimate that the Milky Way galaxy contains between 25 and 100 billion brown dwarfs (with masses $>$0.03 M$_\odot$).

Key words: brown dwarfs – stars: formation – stars: luminosity function, mass function – stars: pre-main-sequence – open clusters and associations: individual: RCW 38.

1 INTRODUCTION

Stellar clusters born embedded in molecular clouds have long been recognized as important laboratories for understanding how star formation works. They give birth to stars across a wide range of masses, from the most massive stars reaching several tens of solar masses to the substellar objects with masses below 0.075 M$_\odot$. The distribution of masses in young clusters, the initial mass function (IMF), is a fundamental outcome of star formation, and therefore has been a topic of extensive research. Measurements of the IMF have been represented in the literature by various functional forms. On the high-mass side, the mass function can be described as a power law $dN/dM \propto M^{-\alpha}$ with the Salpeter slope $\alpha = 2.35$ (Salpeter 1955). As the studies of the solar neighbourhood and the Galactic disc

show, the Salpeter slope seems to be a good approximation of the mass function down to $\sim$0.5 M$_\odot$, but below this mass the distribution becomes significantly flatter (by $\Delta\alpha \sim$1.5; Luhman 2012 and references therein). This leads to updated descriptions of the IMF, such as a lognormal distribution (Chabrier 2005), a set of power-law functions (Kroupa 2001) or a tapered power law (De Marchi, Paresce & Zwart 2005). The flattening of the IMF at the low masses is also seen in young clusters and star-forming regions, which in general yield slopes $\alpha < 1$, for the masses below $\sim$1 M$_\odot$ (e.g. Luhman 2004b, 2007; Bayo et al. 2011; Peña Ramírez et al. 2012; Scholz et al. 2012a; Lodieu 2013; Mužić et al. 2015).

The low-mass end of the IMF is the focus of the SONYC survey – short for *Substellar Objects in Nearby Young Clusters* – our project aiming to provide a complete, unbiased census of the substellar population in nearby star-forming regions. The survey is based on deep imaging on 4–8-m-class telescopes, and followed up with extensive spectroscopic campaigns targeting candidate very-low-mass

objects in four nearby star-forming regions. We reach completeness limits of 0.005–0.01 $M_\odot$ in NGC 1333 and Cha-I, 0.1–0.2 $M_\odot$ in Lupus 3 and ~0.03 $M_\odot$ in ρ-Oph. Thanks to SONYC, and similar recent surveys by other groups, the substellar IMF in nearby regions is now well characterized down to ~10 $M_{\rm Jup}$, and in a few selected regions even deeper (~5 $M_{\rm Jup}$). In SONYC, we find that for every formed brown dwarf (BD), there are two to six stars, and the slope of the mass function below 1 $M_\odot$ is $\alpha \sim 0.7$ (Scholz et al. 2012b, 2013; Mužić et al. 2015). The relatively large range in the star-to-BD number ratio does not necessarily reflect differences between different regions, it is rather caused by uncertainties due to incompleteness of the spectroscopic follow-up, choice of isochrones used to derive masses, uncertainties in distances, etc. The IMF in most star-forming regions appears to be continuous across the hydrogen- and deuterium-burning limits. In a comparative study of seven nearby star-forming regions, Andersen et al. (2008) find that the ratios of stars to BDs are consistent with a single underlying IMF.

While strong IMF variations are excluded for most nearby regions, there might be a few notable exceptions that hint that the environment might after all influence the BD production efficiency. In Scholz et al. (2013), we investigated the mass functions in IC 348 and NGC 1333, two young clusters in Perseus. We find that, under plausible assumptions, the cumulative mass distributions of the two clusters are significantly different, resulting from an overabundance of very-low-mass objects in NGC 1333. In a recent analysis of the same two clusters, Luhman, Esplin & Loutrel (2016) also report a higher abundance of low-mass objects in NGC 1333. This suggests that the relative number of very-low-mass objects in star-forming regions might depend on stellar density, in the sense that regions with higher densities produce more objects with very low masses. Furthermore, in Lupus 3, we find evidence for a turn-down of the IMF in the substellar regime. This cluster seems to produce fewer BDs than other clusters we have studied (Comerón 2011; Mužić et al. 2015).

Most of the star-forming regions where the substellar content was studied in detail are relatively loose groups of low-mass stars, with no or very few massive stars, and mostly similar in their properties. An exception is the Orion nebula cluster (ONC), the only massive star-forming region within 500 pc distance. The ONC low-mass IMF has been a subject of several studies to date, yielding somewhat inconsistent results, from a steeply declining IMF (Da Rio et al. 2012) to an upturn in the low-mass regime (Muench et al. 2002). Most recently, based on the new photometric near-infrared (NIR) observations of the ONC, Drass et al. (2016) derive a bimodal form of an IMF, with a dip around 0.1 $M_\odot$, and two peaks at 0.25 and 0.025 $M_\odot$. A similar, although shallower dip was previously reported in the analysis by Lucas, Roche & Tamura (2005). Drass et al. (2016) interpret the substellar peak as possibly formed by BDs ejected from multiple systems or circumstellar discs at an early stage of star formation.

Environmental difference is in fact theoretically expected, as most of the current BD formation theories predict an overproduction of substellar objects in dense environments, or close to very massive stars. Bonnell, Clark & Bate (2008) investigate the formation of BDs and very-low-mass stars through the gravitational fragmentation of infalling gas into stellar clusters, where these clusters provide the gravitational focus that attracts gas from the surrounding molecular cloud, and provide gas densities that are sufficiently large to form BDs. BDs in this simulation are therefore preferentially formed in regions of high stellar densities. In the largest hydrodynamical simulation of cluster formation to date (Bate 2012), very-low-mass objects are formed by ejection from the reservoir of accretion material, and the efficiency of their formation is expected to depend on density, as higher stellar densities favour ejections. Furthermore, the turbulent fragmentation framework also predicts that an enhancement in density should lead to an increase in the numbers of BDs (Padoan & Nordlund 2002; Hennebelle & Chabrier 2009). Finally, a viable channel for BD formation is in the vicinity of OB stars, whose powerful ionization fronts can erode the outer layers of a pre-stellar core, leaving a small fragment that can only form a substellar object (Whitworth & Zinnecker 2004).

After consolidating the shape of the IMF in most of the nearby star-forming regions, the next logical step to test potential environmental differences in the production of very-low-mass stars and BDs is to analyse their content in some of the massive, dense embedded clusters. The main challenges in studying these clusters are their distances, crowding (in some cases) and high extinctions due to the high column density molecular clouds with which they are associated. As a result, most studies of the stellar content in massive embedded clusters extend down to a few solar masses, and only a few reach close to the hydrogen-burning limit. The recent study in Westerlund 1 by Andersen et al. (2017) extends down to 0.15 $M_\odot$ in the outer parts of the cluster, an unprecedented depth for such a distant cluster (~4 kpc). Similar mass limits have been reached in Trumpler 14 (Rochau et al. 2011). The IMF has been characterized in NGC 3603 down to 0.4 $M_\odot$ (Stolte et al. 2006; Harayama, Eisenhauer & Martins 2008).

In this paper, we present new adaptive optics (AO) observations of the central half parsec of the young embedded cluster RCW 38. Previous deep observations of the core of this cluster reached down to the hydrogen-burning limit (DeRose et al. 2009), and the present data extend this data set further down into the substellar regime. RCW 38 is a young (<1 Myr), embedded cluster surrounding a pair of early O stars, and located at the distance of 1700 pc (Wolk, Bourke & Vigil 2008). The distance to RCW 38 has been derived from the photometry of the OB-star candidates (Muzzio 1979; Avedisova & Palous 1989), and from examining the CO structures in the Vela ridge, in addition to the photometric data (Murphy 1985). The X-ray luminosity function is consistent with the 1700 pc estimate from these works (Wolk et al. 2006). Several works have inferred the very young age of the cluster. Wolk et al. (2006) estimate the age to be 0.5 Myr, with an upper limit of 1 Myr (older age doubles the number of O stars, which the authors find unlikely). Using the NIR and X-ray photometry, Getman et al. (2014) estimate individual ages of several cluster members, giving on average ~1 Myr. The disc fraction of ~70 per cent is also consistent with the same age (Winston et al. 2011). The CO maps of the region reveal that the stellar cluster is associated with two molecular clouds containing the total gas mass of $2.3 \times 10^4 \, M_\odot$, whose collision possibly triggered the recent massive star formation (Fukui et al. 2016). The massive stellar content and the structure of RCW 38 have been characterized as part of the MYStIX project (Kuhn, Getman & Feigelson 2015a), which find that this cluster has the highest projected core surface density among all the clusters in their study (20 massive young clusters within 4 kpc), and twice as high as that of the ONC. The peak core surface density of RCW 38 is found to be ~34 000 stars pc^{-2},[1] compared to ~17 000 stars pc^{-2} in the ONC (Kuhn et al. 2015a), 2000 pc^{-2} in ρ-Oph and ≤1000 pc^{-2} in the remaining star-forming regions covered by SONYC (Gutermuth et al. 2009). The analysis based on the X-ray, NIR and mid-infrared (MIR) data (Wolk

---

[1] We will re-derive the surface densities for the cluster core in Section 4.5.
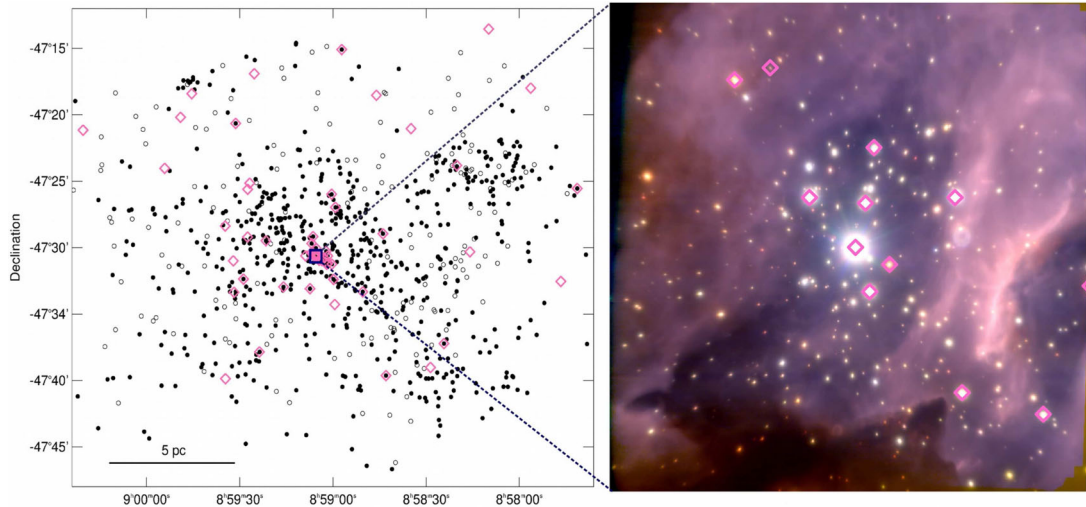
Figure 1. Left: large-scale view of RCW 38. Circles mark the identified Young Stellar Objects (YSOs) (filled) and YSO candidates (open) from Winston et al. (2011), and the diamonds mark OB-star candidates (Wolk et al. 2006; Winston et al. 2011). The field covered by the NACO data is shown close to the centre of the plot. Right: colour-composite image of the central part of RCW 38, from the NACO images in *J* (blue; 2003 data set), *H* (green; 2013 data set) and *Ks* band (red; 2013 data set). The brightest star in the centre of the image is the binary IRS2; the frame size is ∼53 × 51 arcsec^2.

et al. 2006; Winston et al. 2011) identified more than 600 young stellar objects (YSOs), as well as about 60 O- and OB-star candidates located in four sub-clusters, and distributed in the area around them. The total extent of the cluster can be approximated by an ellipsoid with semi-major and semi-minor axes of ∼10 pc × 8 pc (Kuhn et al. 2014). 12 of the OB-star candidates are found in the central core of the cluster studied in this work.

The left-hand panel of Fig. 1 shows a large-scale view of RCW 38, with the circles marking the identified YSOs (filled) and YSO candidates (open) from Winston et al. (2011), and the diamonds marking the OB-star candidates (Wolk et al. 2006; Winston et al. 2011). The small square close to the centre marks the central half parsec of the cluster studied in this work at high angular resolution. At least an order of magnitude denser than the nearby star-forming regions, and rich in massive stars, RCW 38 is an ideal environment to look for potential differences in BD formation efficiency.

This paper is structured as follows. Section 2 contains the details of the observations and data reduction. The data analysis, including the point spread function (PSF) fitting, photometric calibration and completeness analysis, is presented in Section 3. In Section 4, we discuss the cluster membership, derive the mass distribution, test the influence of unresolved binaries on our derivation of the IMF and estimate BD frequencies. In the same section, we also present stellar densities in RCW 38, along with several other nearby star-forming regions. Summary and conclusions are given in Section 5.

2 OBSERVATIONS AND DATA REDUCTION

2.1 NAOS-CONICA/VLT

Observations of RCW 38 were performed using the AO-assisted imager NAOS-CONICA (NACO; Lenzen et al. 2003; Rousset et al. 2003) at the ESO's Very Large Telescope (VLT), under the programme number 090.C-0270. We also use the data available from the ESO archive (programme ID 70.C–0400), previously published in DeRose et al. (2009). The observing setup in both programmes includes the S54 camera, with the pixel scale of 0.054 arcsec and

54 × 54 arcsec^2 field of view (FoV). The S54 camera is accompanied by the instrument mask FLM_100, which attenuates flux towards the edges of the field. The effect is corrected for by the flat-field, except in the corners of the image where the transmission falls below 5 per cent. The details of the observations, including filters and total on-source exposure times, are listed in Table 1. The AO loop was locked on the central binary [FP74] RCW 38 IRS 2. The binary separation is small enough (0.27 arcsec) not to be resolved by the NAOS Shack–Hartmann wavefront sensor.

The data from 090.C–0270 were obtained in service mode, with various observing blocks executed at different nights between 2012 November and 2013 January, and were later combined into a single deep mosaic for each band. The data from 70.C–0400 were obtained in 2003 February. For more details about this data set, please refer to DeRose et al. (2009). In the remainder of the paper, we refer to these two data sets as the '2003 data set' and '2013 data set'.

Standard NIR data reduction techniques were applied using our house-brewed IDL routines, including sky subtraction (obtained on a nearby dark field), flat-fielding and bad-pixel correction. The 2013 data set is affected by the so-called 50 Hz noise, which used to sporadically appear in the data taken with the Aladdin3 detector (operational until 2014 September). The noise manifests itself as a horizontal stripe pattern, variable in intensity and time. The pattern was removed using the procedure described in Hußmann et al. (2012). The shift between the individual exposures was determined using the routine *jitter* from the ECLIPSE package (Devillard 1997), allowing the mosaic construction by a simple shift-and-add.

The colour-composite image of the central region of RCW 38, constructed from the *J*-band (blue; 2003 data set), *H*-band (green; 2013 data set) and *Ks*-band (red; 2013 data set) images, is shown in the right-hand panel of Fig. 1.

2.2 ISAAC/VLT

To estimate the amount of contamination by field stars, we observed a control field, using the NIR camera ISAAC at the VLT (Moorwood et al. 1998). The Hawaii short-wavelength arm of the instrument

Table 1. Summary of the observations.

Object	α (J2000)	δ (J2000)	Date	Instrument	Pixel scale (arcsec)	FoV (arcsec)	Filter	Total exp. time (s)
RCW 38	08:59:05.5	−47:30:43	2013-01-01, 01-12, 01-21, 01-26	NACO	0.054	54	H	6880
RCW 38	08:59:05.5	−47:30:43	2012-11-21, 12-31, 2013-01-01	NACO	0.054	54	Ks	3648
RCW 38	08:59:05.5	−47:30:43	2003-02-23	NACO	0.054	54	J	448
RCW 38	08:59:05.5	−47:30:43	2003-02-23	NACO	0.054	54	H	420
RCW 38	08:59:05.5	−47:30:43	2003-02-23	NACO	0.054	54	Ks	480
Control field	08:54:55.3	−46:46:24	2012-10-26	ISAAC	0.148	152	H	2160
Control field	08:54:55.3	−46:46:24	2012-10-29	ISAAC	0.148	152	Ks	1890

was used to obtain *H*- and *Ks*-band images, providing the FoV of $152 \times 152 \, \text{arcsec}^2$ and pixel scale of $0.148 \, \text{arcsec pixel}^{-1}$. A control field should be far enough from the cluster not to contain any of its stars, but also close enough to trace the same background population. Our control field was chosen to be located about $1°$ away from the centre of the RCW 38 cluster, along the galactic plane. This region is just outside the region of significant CO emission of the Vela Molecular Ridge C (Yamaguchi et al. 1999), far from the dense CO clumps. It is also free of Hα emitters distributed throughout the Vela Molecular Ridge (Pettersson 2008). The control field does not contain sufficiently bright stars that could provide good quality AO correction with NACO (the brightest star has $K_S = 12.0$ and $V = 14.1$). However, the density of stars in the control field images is only $\sim 0.04 \, \text{stars arcsec}^{-2}$, around four times lower than in the cluster field. Therefore, the seeing-limited ISAAC data are suitable to estimate the field star contamination in RCW 38. Also, as we will show in Section 3.4, the control field photometry is deeper than the cluster photometry. The details of the observations are included in Table 1.

Standard data reduction, including sky subtraction (determined from dithered science exposures), flat-field and bad-pixel corrections, and creation of final mosaics were performed using the ESO's ISAAC pipeline, and our own IDL scripts.

3 DATA ANALYSIS

3.1 PSF fitting photometry and astrometry

For the NACO mosaics, photometry and astrometry were obtained using the STARFINDER PSF fitting algorithm (Diolaiti et al. 2000), particularly suitable for the analysis of AO-assisted data in crowded fields. STARFINDER uses an empirical PSF, extracted directly from the imaging data. This is crucial in the case of the AO data, as the shape of the PSF can be extremely complex, especially in the presence of anisoplanatic effects. The method applied in this work is described in detail in Schödel (2010), and we refer the interested reader to this work, containing a detailed justification of the method and particular details of the STARFINDER setup.

In our data, we observe strong anisoplanatic effects towards the edges of the detector, expected given the FoV of ~ 55 arcsec, and the isoplanatic angle in the *H* band of the order of 10 arcsec at 1 arcsec optical seeing. Stars at the edges of the detector are strongly elongated, and using a single PSF in the analysis of AO observations with a relatively large FoV inevitably results in systematic errors in both astrometry and photometry, dependent on the radial distance from the AO guide star (Schödel 2010). The effect is more strongly pronounced in the 2013 data set. We therefore implemented the following approach.

(i) The images were rebinned (oversampled) by a factor of 2, which helps to deal with undersampling of the NACO S54 data. Hav-

ing well-sampled data is a necessary requirement for STARFINDER. We then create a set of moving tiles, each with the size $512 \times 512 \, \text{pixel}^2$ (i.e. $\sim 13.8 \, \text{arcsec} \times 13.8 \, \text{arcsec}$), and each overlapping 75 per cent with the previous one. This results in 13×13 overlapping subfields. The size of the subfields was chosen to be comparable to the size of the isoplanatic angle, while still large enough to have several stars suitable for local PSF extraction.

(ii) Optimal PSF extraction requires several bright, isolated sources to be able to determine not only the central core of the PSF, but also the faint seeing foot further away from the centre. In our case, the brightest stars are located closer to the centre of the image. However, the anisoplanatism will have a much more important effect on the PSF core than on the seeing foot that is caused by the light not corrected by the AO. Therefore, we extracted an initial PSF with well-defined wings, using several very bright, isolated stars close to the cluster centre. We then merged the individual PSF cores extracted from each sub-image, with the wings of the initial PSF. This step is important to avoid strong systematic variations of the zero-point (ZP) across the FoV.

(iii) About 200 stars brighter than $H = 16.5$, distributed across the FoV, were used for the local PSF extraction. Their positions were supplied to STARFINDER, which then performed the local PSF extraction, the merging of each local PSF core with the faint-wing PSF and finally the PSF source extraction for each subfield. Since we designed the fields to have a large overlap, the majority of the sources will be represented in several sub-images. The slightly different subset of stars used for PSF extraction between overlapping sub-images will affect the photometry and astrometry of each individual source. We use the values from the overlapping sub-images to calculate the final flux and position (average), as well as their respective uncertainties. The uncertainties have been derived combining in quadrature the measurement errors supplied by STARFINDER and the standard deviation of values derived from multiple fields. The flux uncertainties given by STARFINDER take into account Gaussian and photon noise of the images. The corners of the image ($128 \times 128 \, \text{pixel}^2$) are represented only once; therefore, only the STAFFINDER errors could be taken into account. However, they do not contain any stars due to the NACO S54 camera's field mask.
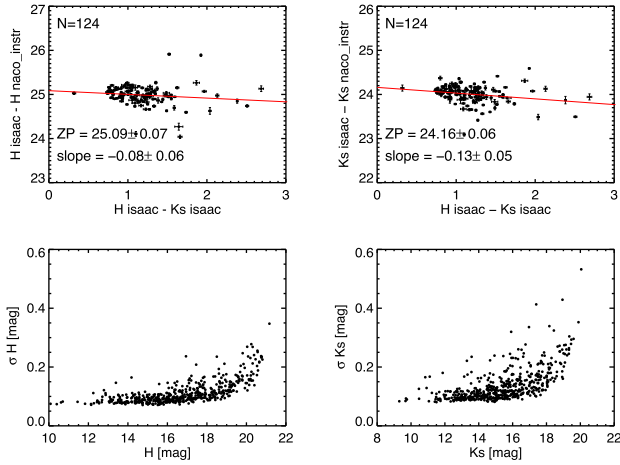
3.2 Photometric calibration

To calibrate our photometry, we use the catalogue from Ascenso et al. (in preparation), extracted from the larger FoV images of RCW 38 obtained by ISAAC/VLT. The seeing-limited ISAAC data suffer more from crowding effects than the NACO data; we have therefore used only matching sources without any neighbour within 0.5 arcsec having a luminosity contrast $\Delta H > 2$ mag. Furthermore, we have rejected objects with uncertainties larger than 0.05 mag in the ISAAC data, and 0.1 mag in the NACO instrumental magnitudes, and took into account only the objects brighter than $Ks = 15$. We fit

Table 2. Parameters of the NACO photometric calibration.

Data set	ZP_1	c_1	ZP_2	c_2	ZP_3	c_3
2003	25.12 ± 0.11	0.02 ± 0.03	25.08 ± 0.09	-0.02 ± 0.03	24.08 ± 0.09	-0.02 ± 0.03
2013	–	–	25.09 ± 0.07	-0.08 ± 0.06	24.16 ± 0.06	-0.13 ± 0.05

Figure 2. Photometric calibration for the main 2013 data set used in this paper. Upper panels: ZP and colour-term fit. Lower panels: photometric uncertainties as a function of magnitude.

the ZPs, as well as the colour terms using the following equations:

$$J = J_{\rm instr} + ZP_1 + c_1 * {\rm colour}$$

$$H = H_{\rm instr} + ZP_2 + c_2 * {\rm colour}$$

$$Ks = Ks_{\rm instr} + ZP_3 + c_3 * {\rm colour}, \tag{1}$$

where colour $= J - Ks$ for the 2003 data set and colour $= H - Ks$ for the 2013 data set (no *J*-band data). In the case of 2013 data set, only the last two equations are valid. The derived ZPs and colour terms are given in Table 2.

The photometric uncertainties were calculated by combining the uncertainties of the ZPs, colour terms and the uncertainties in STARFINDER extraction due to PSF variation described in Section 3.1. Fig. 2 shows the ZP and colour-term fits for the 2013 data set (upper panels), along with the photometric uncertainties as a function of magnitude, for the *H* and the *Ks* bands. The 2013 combined *HKs* catalogue contains 507 objects; 309 of these match with the *JHKs* catalogue from 2003. We note that in the analysis of the common sources we adopt the 2003 *J*-band photometry, combined with the 2013 photometry in *H* and *Ks*.

3.3 Completeness of the photometry

The completeness of our photometry was assessed with an artificial star test. An image containing randomly positioned artificial stars was created with STARFINDER's function *image_model*, taking into account the spatially variable PSF. This image was added to the broad-band mosaic, and the associated photon noise was added in quadrature to the noise image. The resulting image and its noise were used as the input for a routine identical to the one used to obtain the photometry with the spatially variable PSF (described in Section 3.2). We inserted only 100 stars at a time to avoid crowding, and repeated the same procedure 10 times at each magnitude (in steps of 0.25 mag) to improve statistics. The ratio between the number of recovered and inserted artificial stars versus magnitude
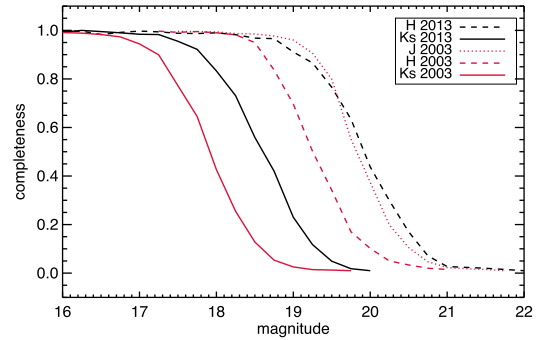
Figure 3. Completeness of the NACO photometry calculated with an artificial star experiment, for the two data sets, with 2013 shown in black and 2003 in red. Different line styles represent different photometric bands: full, dashed and dotted lines for *Ks*, *H* and *J* bands, respectively.

is shown in Fig. 3, for both 2003 (red lines) and 2013 data sets (black lines). The 90 per cent completeness limits are $H = 18.6$ mag and $Ks = 17.2$ mag for the 2003 data set, and $H = 19.1$ mag and $Ks = 17.8$ mag for the deeper 2013 data set. The completeness limits derived for the 2003 data set are deeper than those previously reported by DeRose et al. (2009), likely due to our improved source extraction technique taking into account spatial variability of the PSF.

3.4 Control field photometry

The PSF photometry on the control field data was performed using STARFINDER, employing a single empirical PSF extracted from stars across the field. The photometric ZPs were calculated from the comparison with the 2MASS catalogue (Skrutskie et al. 2006). Stars brighter than $H \sim 14$ and $Ks \sim 13$ might suffer from non-linearity effects and were excluded. We use the sources with 2MASS quality flags C or better (SNR>5 in all three bands), and with 2MASS photometry errors ≤ 0.1 mag. Finally, we keep only the sources without a neighbour within a radius of 3 arcsec, or with one that is more than 2 mag fainter. Due to a relatively small overlap range between the ISAAC and 2MASS catalogues for the control field, we only derive the ZPs for the photometric calibration, ignoring any potential colour terms.

The completeness of the photometry was again assessed using an artificial star test, inserting 100 stars at a time, and repeating the procedure 10 times at each magnitude, in steps of 0.2 mag. The control field photometry is 90 per cent complete at $H = 20.8$ and $Ks = 20.3$. This is 1.7 and 2.5 mag deeper than the 2013 NACO data set in the *H* and *Ks* bands, respectively.

4 RESULTS AND DISCUSSION

4.1 Extinction and stellar masses

Fig. 4 shows the colour–magnitude diagrams (CMD) and the colour–colour diagram (CCD) used to derive the extinction of the sources in RCW 38. Given the young age of the cluster, many
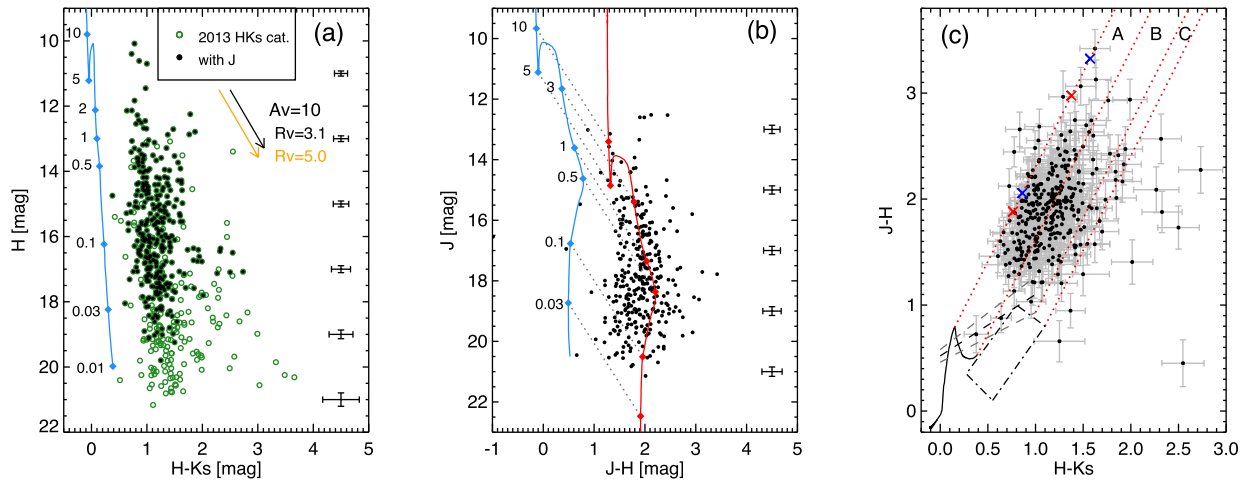
Figure 4. (a) H versus $H - Ks$ colour–magnitude diagram of the sources detected in RCW 38, with the green open circles marking all the sources from the 2013 *HKs* catalogue, and the black dots marking those that also have the *J*-band photometry available. The blue line on the left is the combined PARSEC–BT-Settl 1 Myr isochrone. Two reddening vectors are shown, for $R_V = 3.1$ (black) and $R_V = 5.0$ (orange). (b) J versus $J - H$ colour–magnitude diagram, with the 1 Myr isochrone at $A_V = 0$ (blue) and $A_V = 13$ (average extinction of the cluster for $R_V = 3.1$; red). Note that the isochrone reddened by $A_V = 11.3$ and $R_V = 5.0$ would be identical to the one shown here. (c) Colour–colour diagram. The solid black line represents the evolutionary models (PARSEC–BT-Settl), the dashed black and grey lines represent the locus of T-Tauri stars and the corresponding uncertainties (Meyer, Calvet & Hillenbrand 1997), whereas the dash–dotted rectangle represents the locus of Herbig AeBe stars (Hernández et al. 2005). The dotted red lines are the reddening vectors (Cardelli, Clayton & Mathis 1989). The crosses mark $A_V = 10$ and 20 mag for $R_V = 3.1$ (red) and $R_V = 5.0$ (blue).

objects are expected to host circumstellar discs or envelopes, which in turn can introduce some unknown excess to the intrinsic NIR colours of cluster members. As argued by Cieza et al. (2005), classical T-Tauri stars (CTTSs) can present an excess already in the *J* band, and therefore a simple de-reddening of the photometry to the model isochrones will overestimate the extinction, and consequently also the stellar luminosity. To derive the extinction towards individual stars in the cluster, we therefore develop the following procedure that takes into account a possible intrinsic excess.

(i) Below $1\,M_\odot$, we employ the latest version of the BT-Settl models (Baraffe et al. 2015), while for the more massive stars we use the PARSEC[2] stellar tracks (Bressan et al. 2012; Chen et al. 2014). As can be appreciated from Fig. 4, the transition at $1\,M_\odot$ between the two sets of models is smooth. We assume a distance to the cluster of 1700 pc, an age of 1 Myr, and adopt the extinction law from Cardelli et al. (1989) with the standard value of the total-to-selective extinction ratio $R_V = 3.1$, as well as $R_V = 5.0$, which might be more suitable for dust-rich environments. To estimate the effect that the photometric uncertainties have on our determination of extinction and mass, we apply the Monte Carlo method: for each source, we create a set of 1000 magnitudes in each band, assuming a normal distribution with a standard deviation equal to the respective photometric uncertainty. For each of the 1000 realizations, we then derive the mass and A_V as described below. The final mass and A_V for each source are calculated as an average, and their uncertainties as the standard deviation of all realizations.

(ii) For the sources with the full *JHKs* photometric information (309 objects out of 507 found in the 2013 *HKs* catalogue), we first check the source's position in the CCD diagram. In Fig. 4(c), the solid black line represents evolutionary models, the dashed black and grey lines the locus of T-Tauri stars and the corresponding uncertainties (Meyer et al. 1997), whereas the dash–dotted rectangle represents the locus of Herbig AeBe stars (Hernández et al. 2005).

The dotted red lines are the reddening vectors (Cardelli et al. 1989), encompassing the regions where the colours are consistent with reddened evolutionary models (region A), CTTSs (region B) and Herbig AeBe stars (region C). If the star falls in region A of the CCD, its extinction and corresponding mass are derived by de-reddening its photometry to the 1 Myr isochrone in the *J*, ($J - H$) CMD. In region B, the extinction is derived by de-reddening the colours to the CTTS locus (Meyer et al. 1997). We note that the objects in region A could also be part of the CTTSs; however, the derived A_V differences are typically smaller than the derived uncertainties, and for simplicity we decide to only consider the evolutionary models. The derived extinction is then used to convert the *J*-band photometry to the absolute *J*-band magnitude, which is in turn compared to the models to derive the mass. For the stars in region B, in addition to the interstellar extinction, we also correct for an excess due to the circumstellar disc or envelope, chosen randomly in the interval 0–0.7 mag for the *J* band (Cieza et al. 2005). In the case that the derived mass is larger than $2\,M_\odot$ (upper mass limit for T-Tauri stars), the procedure is repeated by de-reddening the colours to the Herbig AeBe locus (Hernández et al. 2005). The intrinsic colour in this case is a randomly chosen value within the dash–dotted box shown in Fig. 4(c), falling along the reddening line. The same procedure is performed if the object falls within region C. Finally, if the object falls to the left of region A, or to the right of region C, the extinction and mass cannot be derived.

(iii) For the sources without the *J*-band photometry, the extinction is derived from the *H* versus ($H - Ks$) CMD. To account for a possible intrinsic infrared excess, in half of the 1000 realizations for each source, we allow for an intrinsic ($H - Ks$) excess, as a randomly chosen value between 0.4 and 1 mag, and the intrinsic *H*-band excess in the interval 0–1.2 mag. The colour span was chosen according to the intrinsic colours of the CTTSs (Fig. 4c), and the *H*-band excess of CTTSs given in Cieza et al. (2005). The 50 per cent fraction is chosen because about half of the *JHKs* sources are found left of region B in the CCD. The mass is then derived from the absolute *H*-band magnitude.

[2] http://stev.oapd.inaf.it/cgi-bin/cmd
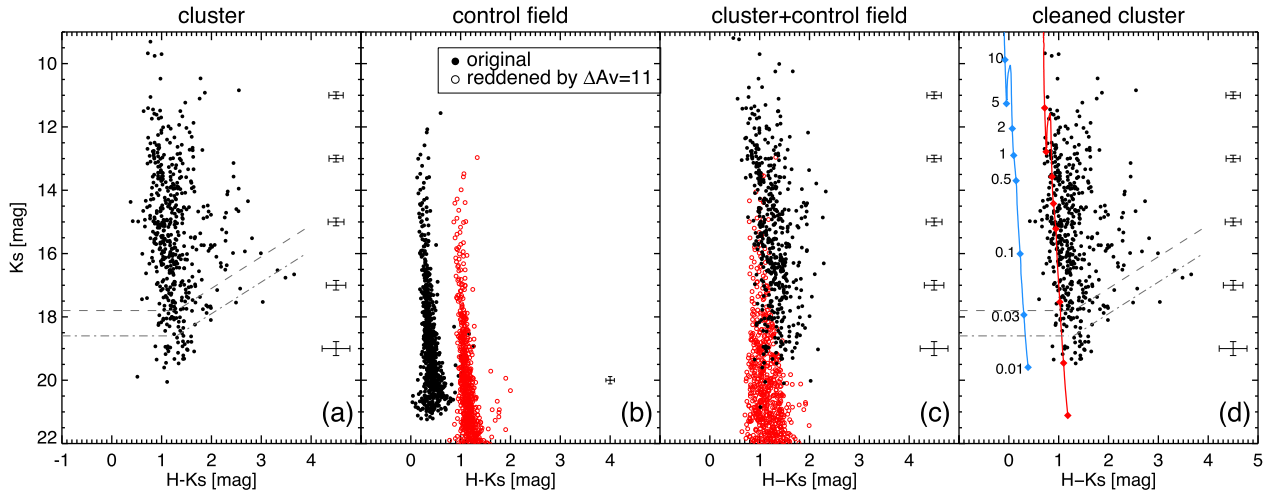
Figure 5. CMD of all the sources detected in RCW 38 (a) and the control field (b). Panel (c) shows the cluster sequence (de-)reddened to the average extinction of the cluster (black), and the control field sequence reddened to the same A_V, and dispersed to match the photometric errors of the cluster field. Panel (d) shows the cluster field after the statistical removal of the contaminants. The 1 Myr isochrones are shown at $A_V = 0$ (blue) and $A_V = 13$ (red; average value of the extinction in the cluster). The grey lines are marking the 90 per cent (dashed) and 50 per cent (dash–dotted) completeness limits.

We note that the spectral types explored in Cieza et al. (2005) range between K0 and M4, while the least massive objects studied here are expected to roughly be ∼M8 (based on the masses we derive). The CTTS sample of Downes et al. (2008) includes three BDs, which show an $H - Ks$ excess of 0.4–0.6 mag. Since we are lacking more information on the NIR excess at the substellar boundary, and since the young BDs share several properties with the CTTSs (e.g. the disc fractions; Dawson et al. 2013), we make an assumption that the values would not be drastically different from those of the low-mass stars.

(iv) The isochrones show a degeneracy at the (pre-)main-sequence transition region in the CMD, for the masses roughly between 3 and 10 $M_\odot$. For stars whose de-reddened photometry falls within this region, all the possible mass/A_V combinations that match the isochrones enter the final calculation of the star's mass and A_V. As a consequence, stars in this mass range have larger relative errors, and cause the slight 'kink' in the IMF at masses around 5–6 $M_\odot$.

The average extinction and the standard deviation for $R_V = 3.1$ are 13.1 mag and 7.4 mag, respectively; for $R_V = 5.0$ the average extinction is 11.3 mag, with a standard deviation of 6.4 mag. It is worth noting that different values of R_V in the NIR do not affect the slopes of the reddening vectors in the Cardelli et al. (1989) formulation of the extinction law (see Fig. 4), but only their length. Therefore, the choice between the two reddening laws affects the estimate of the extinction for individual sources, but has no significant impact on the derived masses.

4.2 Cluster membership

To assess the membership in RCW 38 and statistically correct for the field sources, we compare the cluster CMD with that of the control field. First, the difference in extinction between the two lines of sight has to be taken into account.

The fact that the $H - Ks$ colour has a relatively small scatter for sources of all spectral types allows us to determine an average extinction along any line of sight by assuming an average intrinsic $H - Ks$ for all the observed stars. To determine the average extinc-

tion in the control field, we use the method outlined in Gutermuth et al. (2005). We consider the $H - Ks$ values of the nearest ∼20 stars at each point on a uniform 2 arcsec grid. The extinction at each point of the grid is derived as the 3σ-clipped average of the extinction values derived assuming an average intrinsic $H - Ks = 0.25 \pm 0.07$, and the extinction law of Cardelli et al. (1989). The average intrinsic colour was calculated using the colours of O9–M9 dwarfs from Pecaut & Mamajek (2013), and assuming the underlying mass function from Chabrier (2005). Since we are not looking in the direction of the bulge ($l \sim 267°$), contamination by giants should be small; <3 per cent of the sources along the control field line of sight are expected to be giants or subgiants, according to the Besançon Galaxy model (Robin et al. 2003). Taking into account only the dwarf colours should therefore be a safe assumption.

The average extinction in the control field derived in this way is $A_V = 2.1 \pm 1.1$ mag for $R_V = 3.1$, and $A_V = 1.9 \pm 1.0$ mag for $R_V = 5.0$. The difference between the average extinctions of the cluster and the control field is therefore $A_V \simeq 11$ for $R_V = 3.1$ or $A_V \simeq 9.5$ for $R_V = 5.0$ ($A_{Ks} = 1.3$ in both cases), the amount by which the control field sequence has to be shifted in the CMD before comparison. Panel (a) of Fig. 5 shows all the observed objects in the direction of the cluster field. The grey lines mark the 90 per cent (dash–dotted) and 50 per cent (dashed) completeness limits. The control field CMD is shown in panel (b), with the light grey symbols showing the original photometry derived for this field, and the red ones the same sequence reddened by $A_V = 11$.

The CMD is subdivided into grid cells with a step size of 0.5 mag in both axes. The number of field stars within each cell is normalized to the ratio of the on-sky areas between the cluster and the control field, and corrected for the completeness fractions of the cluster field photometry (the reddened control field photometry is 100 per cent complete below the cluster faint end). The resulting number of objects corresponding to the field object population is then randomly subtracted from corresponding cells of the cluster CMD. However, before the correction, there are two effects that have to be taken into account. The first is the fact that the cluster suffers a significant differential reddening across the field, which means that only the population with extinction close to the average one would be taken into account for the correction. To avoid this, we should (de-)redden
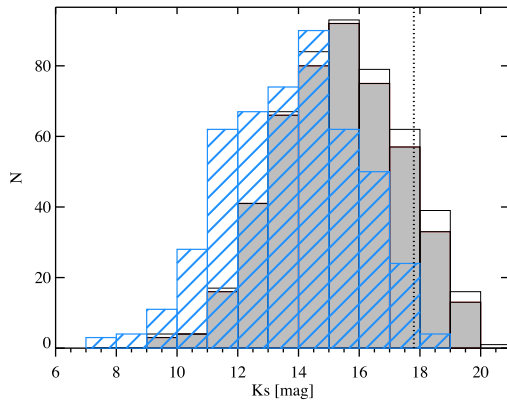
Figure 6. *Ks*-band luminosity function. The white histogram shows all the sources from the *HKs* catalogue, while the grey one shows the probable member sample determined through comparison of the cluster CMD with that of the control field. The blue hatched histogram shows the extinction-corrected version of the grey one. The dotted line marks the 90 per cent completeness limit.

the cluster population to the average cluster extinction ($A_V = 13$ for $R_V = 3.1$). To take into account the uncertainties in A_V, the photometry of each star is de-reddened to a random value within $\pm 1\sigma$ from the average cluster extinction, where σ is the star's A_V uncertainty (black dots in panel (c) of Fig. 5). The sources for which we could not derive the extinction in Section 4.1 have been removed prior to this step (3 out of 507). The second effect is that the control field sequence has significantly lower uncertainties, especially at the faint end, which again will cause some cells to be under- or overcorrected. To fix this, we artificially disperse the control field sequence to match the photometric uncertainties of the cluster field (red dots in panel (c) of Fig. 5). The resulting field-subtracted cluster population is shown in the rightmost panel of Fig. 5, along with the 1 Myr isochrones at $A_V = 0$ (blue) and $A_V = 13$ (red). As evident from Fig. 5, only a small fraction of the sources gets removed from the cluster sequence by this method (~ 5 per cent of the detected objects). As previously discussed by DeRose et al. (2009), the cluster seems to be located in front of a dense molecular cloud whose high extinction screens out background sources. The cleaned cluster sequence contains 476 candidate members.

Fig. 6 contains the *Ks*-band brightness distribution, with the statistically cleaned cluster population shown in grey. The hatched blue histogram contains the same data as the grey one, corrected for extinction. Fitting a Gaussian to the extinction-corrected histogram, we get the peak located at $Ks = 13.9$, which at the distance of 1.7 kpc corresponds to an absolute magnitude of $M_{Ks} = 2.75$, or $\sim 0.4\,\mathrm{M_\odot}$. This is similar to what is seen in other young clusters, e.g. Trumpler 14 (0.4–0.5 $\mathrm{M_\odot}$ at a distance 2.3–2.8 kpc and $\langle A_V \rangle = 3$; Ascenso et al. 2007; Rochau et al. 2011) or Trapezium ($\sim 0.5\,\mathrm{M_\odot}$ for $d = 0.4$ kpc and $\langle A_V \rangle = 9.2$; Muench et al. 2002). It is also in agreement with the simulated *K*-band luminosity function for clusters of non-accreting pre-main sequence (PMS) stars, which peak at $M_K = 2.5$–3 for the ages 0.7–1 Myr (Zinnecker & McCaughrean 1991).

4.3 Initial mass function

To plot the IMF for RCW 38, we take the statistically cleaned probable member masses as derived in previous sections and run a Monte Carlo simulation where each mass is moved by a random offset within its respective $\pm 1\sigma$ uncertainty. This is performed 100 times,

and for each of the 100 realizations we do 100 bootstraps, i.e. random sampling with replacement. In other words, starting from a sample with N members, in each bootstrap we draw a new sample of N members, allowing some members of the initial sample to be drawn multiple times. This results in 10^4 mass distributions, which are used to derive the final IMF and its uncertainties. In Fig. 7, we show the IMF and the corresponding fits in the power-law form $dN/dM \propto M^{-\alpha}$. A Poisson uncertainty is assigned to each fitted data point, but is not shown in the plot for clarity. The lowest masses derived for the objects in the sample are $\sim 0.02\,\mathrm{M_\odot}$, setting the lower limit for the IMF. The data in the lowest mass bins have been corrected for incompleteness, according to the average *Ks*-band magnitude of the sources belonging to it, and the curve shown in Fig. 3. The blue diamonds mark the median of the uncorrected values for the two lowest mass bins, where the correction is significant. We fit a two-segment power law using the least-squares method, with the break masses at 0.2 (left-hand panel in Fig. 7) and 0.5 $\mathrm{M_\odot}$ (middle panel). For a comparison, we overplot the Kroupa segmented power-law IMF, normalized at 0.5 $\mathrm{M_\odot}$ (dashed grey line), with the slopes $\alpha = 2.3$ for $M > 0.5\,\mathrm{M_\odot}$, $\alpha = 1.3$ for $0.08 < M < 0.5\,\mathrm{M_\odot}$ and $\alpha = 0.3$ for $M < 0.08\,\mathrm{M_\odot}$. In the rightmost panel, we show the fit only below $1\,\mathrm{M_\odot}$, to be able to compare it with the IMF fits in the nearby young clusters from the SONYC survey. The summary of the resulting slopes is given in Table 3. The results are largely insensitive to R_V.

On the high-mass side, the slope of the power law in the central $\sim 0.45 \times 0.45\,\mathrm{pc^2}$ of RCW 38 is found to be $\alpha = 1.48 \pm 0.08$, and 1.59 ± 0.13, for the masses above 0.2 $\mathrm{M_\odot}$, and 0.5 $\mathrm{M_\odot}$, respectively. This is lower than the Salpeter slope ($\alpha = 2.35$). A similar slope has been reported in the central regions of other massive clusters. In the central region ($r \le 0.2$ pc) of the Arches cluster, Habibi et al. (2013) find the slope $\alpha = 1.5 \pm 0.35$, while Andersen et al. (2017) report a slope $\alpha = 1.32 \pm 0.16$ in the inner 0.8 pc radius of Westerlund 1. In the inner 0.2 pc radius of NGC 3603, the observed IMF slope is $\alpha \simeq 1.3$ (Stolte et al. 2006; Harayama et al. 2008). In σ Ori, Peña Ramírez et al. (2012) measure a slope $\alpha = 1.7 \pm 0.2$ for masses above 0.35 $\mathrm{M_\odot}$, while in Collinder 69 Bayo et al. (2011) report $\alpha \sim 1.8$ for the mass range 0.65–25 $\mathrm{M_\odot}$. In Arches, Westerlund 1 and NGC 3603, the above-mentioned works all report a steepening of the observed slope at larger radii (to values from 1.8 to Salpeter), which is interpreted as evidence for mass segregation. However, great care should be taken when interpreting these results in distant, rich clusters, because incompleteness due to crowding can produce a similar effect of radially changing slope, even in a completely unsegregated cluster (Ascenso, Alves & Lago 2009). As the latter work shows, a rigorous study of completeness (which is not always found in the literature) is a prerequisite when analysing the radial properties in crowded regions.

In the case of RCW 38, although the crowding does not pose a real problem in the presence of the AO observations, the present work does not allow us to judge whether the cluster is mass segregated, simply because the mass function of the wider RCW 38 is yet to be derived. The combined X-ray (*Chandra*) and MIR (*Spitzer*) observations reveal a presence of four sub-clusters (Winston et al. 2011). The central sub-cluster surrounding the source IRS 2 shows a higher concentration of OB candidates than any of the other three sub-clusters; however, an even larger number of OB candidates are found distributed throughout the extended cluster region. Kuhn et al. (2014) describe the RCW 38 morphology as a 'core–halo' structure, meaning that overall the cluster structure appears unimodal with little substructure around a main cluster, but with an excess of stars near the centre. In Kuhn et al. (2015b), the
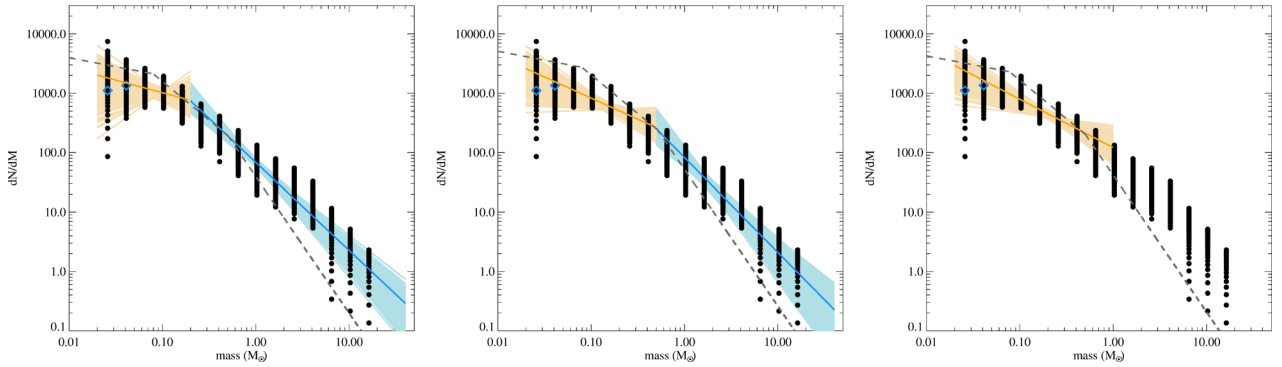
Figure 7. IMF of the central core of RCW 38, represented in the equal-size bins of 0.2 dex in mass. We plot the points (black) and the corresponding fits from 10^4 realizations of the performed Monte Carlo simulation (light blue and orange shaded area). The dark blue/orange lines show the final IMF, with the slopes calculated as a weighted average of the slopes obtained in the simulation. The IMF is represented as a two-segment power law, with different break masses shown in the three panels. The blue diamonds mark the median value of all the realizations without correcting for the completeness, for the bins where it has effect. The grey dashed line is the Kroupa segmented power-law mass function normalized at $0.5\,\mathrm{M_\odot}$.

Table 3. Parametrization of the IMF in RCW 38 in the power-law form, for a selection of different mass break points shown in Fig. 7.

Mass range ($\mathrm{M_\odot}$)	α	α
	$R_V = 3.1$	$R_V = 5.0$
0.2–20	1.48 ± 0.08	1.49 ± 0.09
0.02–0.2	0.42 ± 0.18	0.45 ± 0.18
0.5–20	1.60 ± 0.13	1.60 ± 0.13
0.02–0.5	0.71 ± 0.11	0.72 ± 0.11
0.02–1	0.81 ± 0.08	0.83 ± 0.09

authors estimate the relaxation time for the core, coinciding roughly with the regions studied here, to be ∼5 Myr. For the wider cluster area (∼4.5 pc radius), the relaxation time is much longer, >200 Myr. Given its very young age ($\lesssim$1 Myr), RCW 38 is therefore likely not a dynamically relaxed system.

On the low-mass side, we can compare the results in RCW 38 given in Table 3 with the results of numerous surveys dealing with the low-mass content in nearby star-forming regions and young clusters, including our SONYC survey. To facilitate the comparison, we compile a summary of various results that extend into the BD regime, provided in Table 4. We include mass ranges in the quoted power-law fits, as well as the employed isochrones. The slope α is in agreement between most of the listed star-forming regions and clusters. Our results in RCW 38 are also similar to what is found in other regions, i.e. our data leave no evidence for an effect that a combination of high stellar densities and OB-star presence might have on efficiency of BD/very-low-mass star production.

The only cluster with comparable age and stellar density to RCW 38, and studied in the substellar regime so far is the ONC. Despite being one of the best studied young clusters in general, its low-mass IMF remains controversial. There have been several proposals of a bimodal mass function, with a second peak, or a hint of it, in the substellar regime (Muench et al. 2002; Slesnick, Hillenbrand & Carpenter 2004; Lucas, Roche & Tamura 2005; Drass et al. 2016), where only the work of Slesnick et al. (2004) includes spectroscopic confirmation of the substellar candidates. Da Rio et al. (2012) report an IMF that declines steeply in the substellar regime, with a negative α slope, in contrast to $\alpha \sim$ 0.3–0.6 reported by Muench et al. (2002) and Weights et al. (2009). Possible expla-

nations for these discrepancies include membership issues, issues with understanding survey completeness, different methodologies [optical versus infrared photometry, (non-)existence of the spectroscopic follow-up, adoption of different isochrones and extinction laws], as well as the distance uncertainties (values between 400 and 480 pc assumed in the mentioned works). Moreover, Andersen et al. (2011) report a gradient in the number ratio of stars (0.08–1 $\mathrm{M_\odot}$) to BDs (0.03–0.08 $\mathrm{M_\odot}$), suggesting that the low-mass content of the cluster is mass segregated. Significantly, different areas covered in some of the above-mentioned surveys might therefore influence the derived mass functions to some extent. Finally, there might be an additional complication in the ONC, in the form of a slightly older (4–5 Myr) population located in front of the Orion A cloud (Alves & Bouy 2012; Bouy et al. 2014). This population overlaps significantly with the ONC, and can make up for more than 10–20 per cent of the ONC population, and even 30–60 per cent excluding the Trapezium cluster (Alves & Bouy 2012). Given the youth of the foreground population, and the similarity of its radial velocity to that of the Trapezium population, the membership analysis is far from trivial, and probably affects the IMF determination.

As evident from Table 4, the slope α of the mass function in the power-law form $dN/dM \propto M^{-\alpha}$ is larger than zero, in contrast to the analysis by Andersen et al. (2008). Based on the number ratios of stars to BDs in seven different star-forming regions, they conclude that the substellar IMF turns over with a slope $\alpha < 0$. The reason for this inconsistency might be an overestimate of star-to-BD ratios for some of the clusters, due to incompleteness and/or small number statistics. For example, for IC 348, Andersen et al. (2008) quote a ratio of ∼8, while the newer surveys yield the values 3–4 (Scholz et al. 2013).

Finally, it is worth mentioning that most mass functions that we compare here are system mass functions, with no correction for unresolved binaries, justifying a direct comparison with the RCW 38 IMF. On the other hand, the differences between the system and a single-star IMF are definitely worth exploring, which is what we do in Section 4.6.

4.4 Star/BD ratio

A useful quantity for the comparison of IMF measurements from different surveys is the number ratio of stars to BDs. To estimate the ratio, we use masses derived in Section 4.1, and apply the

Table 4. Power-law slope α of the low-mass IMF in various star-forming regions ($\mathrm{d}N/\mathrm{d}M \propto M^{-\alpha}$).

Region	Mass range ($\mathrm{M}_\odot$)	α	Isochrones	Reference
NGC 1333	0.005–0.60	0.6 ± 0.1	NextGen + Dusty	Scholz et al. (2012a)
	0.030–1.00	0.9–1.0	BT-Settl, Dusty, NextGen	Scholz et al. (2013)
Chamaeleon-I	0.005–1.00	0.78 ± 0.08	BT-Settl	Mužić et al. (2015)
Lupus 3	0.020–1.00	0.79 ± 0.13	BT-Settl	Mužić et al. (2015)
Collinder 69	0.010–0.65	0.18–0.38	Siess + Cond	Bayo et al. (2011)
σ Ori	0.006–0.35	0.55 ± 0.20	Dusty + Cond	Peña Ramírez et al. (2012)
	0.006–0.35	0.68 ± 0.23	Dusty + Cond + Siess	Peña Ramírez et al. (2012)
	0.006–0.11	0.6 ± 0.2	Dusty + Cond + NextGen	Caballero et al. (2007)
	0.012–0.10	0.7 ± 0.3	Dusty + Cond + NextGen	Béjar et al. (2011)
IC 348	0.012–0.075	0.7 ± 0.4	Dusty	Alves de Oliveira et al. (2013)
	0.030–1.00	0.7–0.8	BT-Settl, Dusty, NextGen	Scholz et al. (2013)
ρ Oph	0.004–0.075	0.7 ± 0.3	Dusty	Alves de Oliveira et al. (2012)
ONC	0.030–0.30	-0.12 ± 0.90	NextGen	Da Rio et al. (2012)
	0.020–0.17	-1.41 ± 0.25	DM97	Da Rio et al. (2012)
	0.006–0.10	0.31 ± 0.11	NextGen + Dusty	Lucas et al. (2005)
	0.025–0.12	$\simeq 0.3$	DM97	Muench et al. (2002)
	0.012–0.15	0.3–0.6	NextGen + Dusty	Weights et al. (2009)
Upper Scorpius	0.009–0.2	0.45 ± 0.11	BT-Settl	Lodieu (2013)[a]

BT-Settl: Allard, Homeier & Freytag (2011); Siess: Siess, Dufour & Forestini (2000); COND: Baraffe et al. (2003); Dusty: Chabrier et al. (2000); NextGen: Baraffe et al. (1998); DM97: D'Antona & Mazzitelli (1997).

Note. [a]Using the 5 Myr isochrone.

same method as we did in deriving the IMF, generating 10^4 mass distributions. For the stellar–substellar mass boundary, we take the value at the solar metallicity, $0.075\,\mathrm{M}_\odot$. The low-mass limit on the BD side is fixed to $0.03\,\mathrm{M}_\odot$, and the upper limit for the stellar mass range is chosen to be $1\,\mathrm{M}_\odot$. These limits have been chosen to match those most commonly used in the literature. We derive the star-to-BD number ratio in RCW 38 of 2.0 ± 0.6. The large relative uncertainty of the ratio is mostly due to the incompleteness levels on the low-mass side, and the photometric uncertainties at the star–BD border. The star-to-BD ratio in RCW 38 is similar to that of NGC 1333 (1.9–2.4; Scholz et al. 2013), somewhat lower than that of IC 348 (2.9–4; Scholz et al. 2013), and overlaps with the lower values of the range calculated for Cha-I and Lupus 3 (2.5–6.0; Mužić et al. 2015). However, as pointed out in Mužić et al. (2015), the numbers in Cha-I and Lupus 3 might in reality be on the lower side of the quoted span, as suggested by the analysis based on the completeness levels of the spectroscopic follow-up.

4.5 Comparison of stellar densities

In Section 4.3, we compare the low-mass IMF in RCW 38 to the mass functions found in other (less dense) nearby star-forming regions. In this section, we try to quantify the differences in the stellar densities between several regions. We calculate the stellar surface and volume densities in RCW 38, and three well-studied nearby clusters, Chamaeleon-I, NGC 1333 and the ONC, representing the loose, intermediate and dense stellar environments, respectively. The area for the calculation has a radius of 0.2 pc, which is dictated by the FoV of the RCW 38 data set. For the volume densities, we assume a uniform, spherical distribution with the radius of 0.2 pc. Given the relatively small radius used in the calculation, the values derived here can be considered core densities for each cluster.

We take into account only stars more massive than $0.1\,\mathrm{M}_\odot$, to avoid errors due to incompleteness. For RCW 38, we use the masses calculated in this work. For Cha-I, we consider the masses calculated in Mužić et al. (2015), which are based on the census combined from several works (Luhman 2004a, 2007; Luhman & Muench 2008; Daemgen et al. 2013; Mužić et al. 2015). For NGC 1333, we take

the census from Luhman et al. (2016), and exclude all the objects with the spectral type M7 or later. An M7 object should have the $T_{\mathrm{eff}} \sim 2900\,\mathrm{K}$ (Mužić et al. 2014), equivalent to $0.1\,\mathrm{M}_\odot$ at 1 Myr, according to the BT-Settl models. The NIR sources without spectral classification brighter than $Ks = 12.2$ are kept, since they are expected to be more massive than $0.1\,\mathrm{M}_\odot$ already at $A_V = 0$. There are several YSOs detected only in the MIR, which might be embedded protostars. Excluding or including these sources gives us a range of densities for NGC 1333. For the ONC, we take the masses from Da Rio et al. (2012), using the Baraffe et al. (1998) models.

For RCW 38, the centre is set to the brightest object, the IRS2 binary. At the distance of 1700 pc, we obtain the stellar surface density $\Sigma \sim 2500\,\mathrm{pc}^{-2}$ and stellar volume density $\rho \sim 16\,500\,\mathrm{pc}^{-3}$. This is about six times lower than the average surface density within the same region found by Kuhn et al. (2015a, $\Sigma = 15\,800$ stars pc^{-2}). The discrepancy might be caused by the correction of the surface density maps with the spatially dependent detection fraction in Kuhn et al. (2015a), which are derived from the X-ray observation, and typically drop at the positions of cluster cores. Cha-I has no obvious centre looking at the overall region, and consists of two regions with stellar clustering. We take the centres of the two parts as defined in King et al. (2012a), and get $\Sigma \sim 95\,\mathrm{pc}^{-2}$ and $\rho \sim 640\,\mathrm{pc}^{-3}$ for the northern component, and $\Sigma \sim 70\,\mathrm{pc}^{-2}$ and $\rho \sim 480\,\mathrm{pc}^{-3}$ for the southern component, assuming the distance of 160 pc. Similar to Cha-I, NGC 1333 does not have a well-defined centre: we consider two regions with the highest concentration of members: the first one is centre on the bright F-type star located at 03:29:10.38, +31:21:59.2, while the other is centred at 03:28:57, +31:16:50.9. We assume a distance of 300 pc, and obtain $\Sigma \sim 180$–$220\,\mathrm{pc}^{-2}$ and $\rho \sim 1200$–$1450\,\mathrm{pc}^{-3}$. For the ONC, we centre the field to the centre of the Trapezium cluster, adopt the distance of 400 pc, and obtain $\Sigma \sim 1000\,\mathrm{pc}^{-2}$ and $\rho \sim 6800\,\mathrm{pc}^{-3}$. We note that the values for ONC are in agreement with those calculated by King et al. (2012a), while those for Cha-I are slightly higher due to the updated census used here.

The central part of RCW 38 is therefore more than two times denser than the ONC, an order of magnitude denser than NGC 1333, and about 25 times denser than Cha-I.

4.6 Effect of the unresolved binaries on the IMF

A significant fraction of stars host one of more companions, which, in the case they are unresolved, might affect our determination of the IMF. In this section, we model this effect and the uncertainty it has on the IMF, assuming certain binary frequencies and mass ratios (described below), as well as excluding the possibly resolved wide systems.

4.6.1 Binary frequencies

King et al. (2012a,b) collected binary statistics for seven young star-forming regions, with the separation range of 62–620 au and primary mass range of 0.1–3.0 $M_{\odot}$ being directly comparable between five of them. In this separation range, the lowest density region, Taurus, has a binary fraction of ∼21 per cent, while the other four regions, with densities greater than a few 100 stars pc^{-3} (including the ONC), show a lower fraction of ∼10 per cent. Since the density of RCW 38 is comparable to that of the ONC, and given that this is one of the most thoroughly studied nearby regions, we will use the available ONC statistics for our assumptions on the binary properties of the RCW 38 population.

Köhler et al. (2006) studied the multiplicity properties for 275 objects in the ONC, in the separation range 60–500 au. In the core of the cluster, they find the binary fraction of 2.3 ± 3.0 per cent in the mass range 0.1 $M_{\odot} \leq M \leq 2\,M_{\odot}$, and 21.1 ± 10.2 per cent for $M \geq 2\,M_{\odot}$. The most massive star in their sample has a mass estimate of 16 $M_{\odot}$. Based on a sample of ∼780 ONC members, Reipurth et al. (2007) derive the binary fraction of 8.8 ± 1.1 per cent, in the separation range 67.5–675 au. Although they give no information of the mass range that was studied, almost all identified binaries with existing spectral type estimate have spectral types K–M. In a recent work based on the *Hubble Space Telescope* data, Kounkel et al. (2016b) analyse 324 protostars and PMS stars in Orion (not only the ONC), and find a companion fraction[3] of 10.3 ± 1.0 per cent in the separation range 100–1000 au. Interestingly, they also find a higher companion fraction in denser regions (∼13.5 per cent versus ∼8 per cent for stellar surface density $\Sigma > 45$ and $<45\,\mathrm{pc}^{-2}$, respectively), in contrast to the results of Köhler et al. (2006).

Considering binaries closer than the visual ones studied in the works mentioned so far, there are several studies dealing with spectroscopic binaries in Orion. Morrell & Levato (1991) find that the binary frequency for periods shorter than 100 d ($\lesssim 1$ au for a BV star) among the main-sequence members of the association is 32 per cent. The majority of the studied stars are massive, predominantly BV type. On the other hand, Abt, Wang & Cardona (1991) find the binary frequency among the 26 brightest ONC members (spectral types O6–A1) to be 15 per cent. Kounkel et al. (2016a) find the multiplicity frequency of 5.8 ± 1.1 per cent, for a sample of (typically) K-type stars, i.e. on average lower mass than the previous two samples, and up to 10 au separation. From the high-resolution optical interferometry of a small sample of nine brightest stars in the ONC (A0–O5.5), Grellmann et al. (2013) find six multiple systems, and conclude that the massive stars in the ONC have a companion fraction five times higher than the low-mass stars. The separations probed in this work are ∼1–80 au, filling the gap between the close binaries probed by the radial velocities and AO surveys.

We note that the works dealing with visual binaries normally assume that the projected separation represents the true semi-major axis, although this is statistically not exactly correct (Kuiper 1935). Also, they typically do not correct for the fact that at inclined orbits, a companion will appear for a certain fraction of its period at projected separations shorter than the spatial resolution of the observations. However, as we will show in Section 4.6.3, for our resolution limit of 270 au, this correction should be around 10–15 per cent. For the ONC surveys, which probe much shorter separations, this number will be even smaller; therefore, it is probably safe to ignore it.

In summary, stars more massive than ∼2 $M_{\odot}$ have binary frequency estimates varying between 15 and 60 per cent. On the low-mass side, both close (<10 au) and wide (>60 au) companions in the ONC appear with the frequency of 5–10 per cent. In the separation range of 10–60 au, however, we have no available data for the ONC. For the main-sequence stars and field BDs, the orbital period distribution can be approximated with a lognormal distribution that peaks at ∼5 au for stars with the spectral type M or later, and at ∼45 au for FGK stars (Duchêne & Kraus 2013). We might therefore be missing a substantial number of binaries in the separation range not covered by the current surveys. For this reason, we also test the binary frequency of 20 per cent.

4.6.2 Mass ratios

Given the uncertainties in mass determinations in young clusters, mass ratio distribution q might be a more complex parameter to probe than the binary frequency. In a review paper on stellar multiplicity, Duchêne & Kraus (2013) show that the distribution of mass ratios (in form $\mathrm{d}N/\mathrm{d}q \propto q^{\gamma}$) down to $q \sim 0.1$ for all masses above 0.3 $M_{\odot}$ is essentially flat ($\gamma \sim 0$), whereas below this limit it becomes increasingly skewed towards high-q systems ($\gamma \sim 3$).

4.6.3 Resolved wide systems

The resolution of the NACO data is on average ∼160 mas (calculated as $2 \times$ FWHM of the variable PSFs across the field), which is equivalent to ∼270 au at the distance of 1.7 kpc. To determine how many wide multiple systems we might have detected in our images, we searched for candidate companions within 0.5 arcsec (≈850 au) of each source in the NACO images. We identify 32 potential binary and triple systems (35 if we count the three triples as two binaries each), with the separations between 290 and 820 au, and the median of 590 au. Of the 32 systems, 20 have estimated primary masses below 2 $M_{\odot}$. First, we have to explore the possibility that these are line-of-sight pairs rather than genuine binaries. To do so, we determine the stellar surface density Σ in an area with a radius of 10 arcsec (≈17 000 au) around each candidate primary, and calculate the probability P of finding an unrelated star within a distance θ from each primary by $P = 1 - \mathrm{e}^{-\pi\theta^2\Sigma}$ (Correia et al. 2006; Reipurth et al. 2007), where $\theta = 0.5$ arcsec. We find a non-negligible probability of chance alignment for all our candidates, between 7 per cent and 26 per cent, with an average of ∼20 per cent. This means that ∼26 of the detected pairs might be physical binaries. Since in this analysis we deal with projected separations, rather than true binary orbit sizes, we might also ask how many of the visual binaries we miss due to inclination effects, where a companion appears, for a certain fraction of its period, at projected separations shorter than the spatial resolution of the observations. To estimate how often this happens, we set up a simple geometric simulation in which a set of circular orbits with semi-major axis 270–1100 au is run through a set of inclinations.

---

[3] Given that only 2 out of 57 identified multiple systems are higher order systems (triples), the binary and companion fractions should be similar in this case.

Table 5. Results of the single-star IMF simulation, for a set of different binary frequencies. The system IMF is shown for comparison.

Case	Binary fraction		α				
			0.02–0.2 M$_\odot$	0.2–20 M$_\odot$	0.02–0.5 M$_\odot$	0.5–20 M$_\odot$	0.02–1 M$_\odot$
System IMF			0.42 ± 0.18	1.48 ± 0.08	0.71 ± 0.11	1.60 ± 0.13	0.81 ± 0.08
I	$M < 2$ M$_\odot$	0.05	0.42 ± 0.19	1.50 ± 0.08	0.69 ± 0.11	1.62 ± 0.13	0.80 ± 0.09
	$M \geq 2$ M$_\odot$	0.15					
II	$M < 2$ M$_\odot$	0.10	0.45 ± 0.17	1.50 ± 0.08	0.73 ± 0.11	1.62 ± 0.12	0.83 ± 0.09
	$M \geq 2$ M$_\odot$	0.15					
III	$M < 2$ M$_\odot$	0.10	0.46 ± 0.17	1.57 ± 0.09	0.73 ± 0.10	1.76 ± 0.13	0.83 ± 0.08
	$M \geq 2$ M$_\odot$	0.30					
IV	$M < 2$ M$_\odot$	0.10	0.46 ± 0.18	1.58 ± 0.09	0.75 ± 0.11	1.78 ± 0.14	0.82 ± 0.09
	$M \geq 2$ M$_\odot$	0.60					
V	$M < 2$ M$_\odot$	0.20	0.51 ± 0.17	1.59 ± 0.09	0.77 ± 0.11	1.77 ± 0.13	0.85 ± 0.09
	$M \geq 2$ M$_\odot$	0.60					

The upper limit comes from our chosen upper separation limit of 850 au, multiplied by the average ratio between the semi-major axis and its projected separation for an ensemble of binaries, which is 1.3 (Kuiper 1935). We find that the probability of the two components being at projected distances below 270 au is ∼10 per cent. Therefore, ∼18 low-mass and ∼11 high-mass visual binaries should be excluded from our simulation. We can repeat the same analysis for the range of up to 620 au (useful for the comparison with King et al. 2012b, see below): we find 20 multiple systems, of which ∼11 per cent are chance alignments, and ∼15 per cent are missing due to the projection effects.

Comparing the separation distribution for seven star-forming regions, King et al. (2012b) find that regions with higher densities exhibit a similar proportion of wide (300–620 au) relative to close (62–300 au) binaries, which might be unexpected from the preferential destruction of wider pairs. Binaries with separation 300–620 au comprise 10–40 per cent of the total binary populations in the seven regions studied in King et al. (2012b), with the ONC value being ∼25 per cent. In RCW 38, we detect 20 candidate multiple systems, of which 10 have primary masses >2 M$_\odot$. Subtracting the probable chance alignments, we get the multiplicity frequency in the 300–620 au range of 10/147 and 10/360, for the high- and low-mass bins, respectively. Assuming that these comprise 25 per cent of all the 60–620 au binaries would imply total binary frequencies in this mass range of ∼27 per cent for masses >2 M$_\odot$, and ∼11 per cent for masses <2 M$_\odot$. This is roughly in agreement with the binary frequencies in the ONC listed in the previous section.

4.6.4 IMF simulation

We test the following cases in our simulation: for the low-mass stars (<2 M$_\odot$), we test binary fractions of 5 per cent, 10 per cent and 20 per cent, whereas for the stars with masses >2 M$_\odot$, we test binary fractions of 15 per cent, 30 per cent and 60 per cent. From our candidate member catalogue of masses, we randomly select a fraction that will be split into binaries. For the selected sources with mass <0.3 M$_\odot$, we generate a mass ratio distribution according to $dN/dq \propto q^\gamma$, where $\gamma = 3$, which prefers equal-mass binaries. For masses >0.3 M$_\odot$, we assume a flat mass ratio distribution ($\gamma = 0$). Mass ratios are assumed to have values in the range 0.1–1. The selected sources are then split into binaries according to the corresponding mass ratio, with a requirement that the sum of the expected fluxes for the two components matches the flux of the observed unresolved system. For simplicity, we keep the same A_V as previously derived. The next step is to exclude the detected wide binary systems, by removing 11 randomly selected binaries in the

high-mass bin, and 18 in the low-mass one, as derived in the previous section.

With this new set of masses, we repeat a similar Monte Carlo simulation as the one described in Section 4.3. Starting from the same catalogue as before, each mass is moved by a random offset within its respective ±1σ uncertainty. This is performed 100 times, and in each step a new subset of binaries is generated as described above. For each of these 100 realizations, we do 100 bootstraps. The results for the same mass intervals as those given for the system IMF (Table 3) are shown in Table 5. By comparing the numbers derived for the system IMF with the results of this simulation, we see that unresolved binaries cause the slope on both high-mass and low-mass side to appear flatter than if the binaries were resolved. However, the effect is not very pronounced, with the power-law indices of the single-star IMF and the system IMF agreeing within the errors.

5 SUMMARY AND CONCLUSIONS

In this work, we have presented new, deep AO observations of the central ∼0.5 pc of the young, embedded cluster RCW 38, taken with NACO/VLT. The depth of the data allowed us to extend the analysis of the IMF to the substellar regime for the first time in this cluster, and to our knowledge in any other massive young cluster at the distance above 1 kpc. The analysis is facilitated by the fact that the cluster sits in front of a dense molecular cloud, which blocks the light from most of the background sources. The comparison with the control field shows that ∼96 per cent of the observed objects are expected to be cluster members.

The main goal of this work was to study the low-mass part of the IMF, and compare it with the well-studied mass distributions in nearby star-forming regions. According to various BD formation theories, stellar density is expected to affect the production of very-low-mass objects (high densities favour higher production rate of BDs), as well as the presence of massive OB stars capable of stripping the material around nearby pre-stellar cores until leaving an object not massive enough to form another star. In addition to the theoretical expectations, we discussed several observational hints for environmental differences in the nearby star-forming regions from the literature, which, however, require further investigation. To that end, we choose to study a cluster that is several orders of magnitude denser than any of the nearby star-forming regions (except for the ONC), and also, unlike them, rich in massive stars.

Based on the sample of 476 candidate cluster members, we derive the IMF in RCW 38 between 0.2 and 20 M$_\odot$, and fit a two-segment power law. For the masses in the range 0.5–20 M$_\odot$, we find the slope $\alpha = 1.60 \pm 0.13$, shallower than the Salpeter slope ($\alpha = 2.35$), but

in agreement with several other works, mainly in the centres of the mass-segregated cores of Milky Way's starburst clusters. At the low-mass side, we find $\alpha = 0.71 \pm 0.11$ for masses between 0.02 and $0.5\,\mathrm{M_\odot}$, or $\alpha = 0.81 \pm 0.08$ for masses between 0.02 and $1\,\mathrm{M_\odot}$. This is in agreement with the values found in other young star-forming regions, leaving no evidence for environmental differences in the efficiency of the production of BDs and very-low-mass stars possibly caused by high stellar densities or a presence of numerous massive stars.

We investigate the effects that the unresolved binaries might have on the IMF slope, assuming the binary properties similar to the ONC, and excluding the resolved wide multiple systems. Our Monte Carlo simulation reveals that the unresolved binaries affect the resulting IMF slope, by making the system IMF shallower. However, the effect is not very pronounced, with the power-law indices of the single-star IMF and the system IMF agreeing within the errors.

With the inclusion of RCW38, star-forming regions covering a wide range of initial conditions have now been investigated in the substellar domain. In all regions studied so far, the star/BD ratio is between 2 and ∼5, i.e. for each 10 low-mass stars between two and five BDs are expected to be formed. This is also consistent with estimates of the star/BD ratio in the field (∼5; Bihain & Scholz 2016). The sum of these results clearly shows that BD formation is a universal process and accompanies star formation in diverse star-forming environments across the Galaxy.

By combining previous measurements from the literature, Licquia & Newman (2015) present improved estimates of several global properties of the Milky Way, including its current star formation rate (SFR) of $1.65 \pm 0.19\,\mathrm{M_\odot\,yr^{-1}}$. To do so, they assume an underlying Kroupa IMF (Kroupa 2001), which has an average stellar mass of ∼$0.4\,\mathrm{M_\odot}$ (Marks & Kroupa 2012). The Milky Way therefore forms on average 4 ± 0.5 stars each year, which yields the present BD formation rate of 0.7–2.3 objects per year. Assuming that the BD formation rate remained the same through the age of the Galaxy yields the number of BDs in the Milky Way between 10 and 30 billion. However, as suggested by several works, the SFR of the Galaxy seems to have been larger in the past. Simulations from the latest version of the Besançon Galaxy model (Czekaj et al. 2014), in comparison to the Tycho-2 catalogue data, result in the SFR that decreases with time, no matter which IMF is assumed. In their case, the best fit to the data is provided by the exponentially decreasing star formation rate $\mathrm{SFR}(t) \propto \exp(-\gamma t)$, where $\gamma = 0.12$, t is the time and $t_{\mathrm{max}} = 12.54\,\mathrm{Gyr}$ (Aumer & Binney 2009). Snaith et al. (2015) developed a chemical evolution model to reconstruct the star formation history of the Milky Way's disc. Their SFR shows two distinct phases that correspond to the formation of the thick and the thin discs. The thick-disc formation lasts 4–5 Gyr, during which the SFR reaches 10–15 $\mathrm{M_\odot\,yr^{-1}}$. After this first phase, star formation stalls for about 1 Gyr and then resumes for the thin-disc phase at a level of 2 $\mathrm{M_\odot\,yr^{-1}}$ for the remaining 7 Gyr.

If we assume the BD formation rate behaving in the same way as the SFR, and again assuming the star/BD ratio of 2–5, we arrive at the total number of BDs in the Galaxy of 24–60 billion for the exponentially decaying SFR, and 30–100 billion for the two-phase disc formation model. These numbers should be considered as a lower limit, because the star/BD ratio used in the calculation was derived only for the BDs more massive than $0.03\,\mathrm{M_\odot}$.

ACKNOWLEDGEMENTS

REFERENCES

Abt H. A., Wang R., Cardona O., 1991, ApJ, 367, 155

Allard F., Homeier D., Freytag B., 2011, in Johns-Krull C., Browning M. K., West A. A., eds, ASP Conf. Ser. Vol. 448, 16th Cambridge Workshop on Cool Stars, Stellar Systems, and the Sun. Astron. Soc. Pac., San Francisco, p. 91

Alves J., Bouy H., 2012, A&A, 547, A97

Alves de Oliveira C., Moraux E., Bouvier J., Bouy H., 2012, A&A, 539, A151

Alves de Oliveira C., Moraux E., Bouvier J., Duchêne G., Bouy H., Maschberger T., Hudelot P., 2013, A&A, 549, A123

Andersen M., Meyer M. R., Greissl J., Aversa A., 2008, ApJ, 683, L183

Andersen M., Meyer M. R., Robberto M., Bergeron L. E., Reid N., 2011, A&A, 534, A10

Andersen M., Gennaro M., Brandner W., Stolte A., de Marchi G., Meyer M. R., Zinnecker H., 2017, A&A, 602, A22

Ascenso J., Alves J., Vicente S., Lago M. T. V. T., 2007, A&A, 476, 199

Ascenso J., Alves J., Lago M. T. V. T., 2009, A&A, 495, 147

Aumer M., Binney J. J., 2009, MNRAS, 397, 1286

Avedisova V. S., Palous J., 1989, Bull. Astron. Inst. Czech., 40, 42

Baraffe I., Chabrier G., Allard F., Hauschildt P. H., 1998, A&A, 337, 403

Baraffe I., Chabrier G., Barman T. S., Allard F., Hauschildt P. H., 2003, A&A, 402, 701

Baraffe I., Homeier D., Allard F., Chabrier G., 2015, A&A, 577, A42

Bate M. R., 2012, MNRAS, 419, 3115

Bayo A. et al., 2011, A&A, 536, A63

Béjar V. J. S., Zapatero Osorio M. R., Rebolo R., Caballero J. A., Barrado D., Martín E. L., Mundt R., Bailer-Jones C. A. L., 2011, ApJ, 743, 64

Bihain G., Scholz R.-D., 2016, A&A, 589, A26

Bonnell I. A., Clark P., Bate M. R., 2008, MNRAS, 389, 1556

Bouy H., Alves J., Bertin E., Sarro L. M., Barrado D., 2014, A&A, 564, A29

Bressan A., Marigo P., Girardi L., Salasnich B., Dal Cero C., Rubele S., Nanni A., 2012, MNRAS, 427, 127

Caballero J. A. et al., 2007, A&A, 470, 903

Cardelli J. A., Clayton G. C., Mathis J. S., 1989, ApJ, 345, 245

Chabrier G., Baraffe I., Allard F., Hauschildt P., 2000, ApJ, 542, 464

Chabrier G., 2005, Astrophys. Space Sci. Libr., Vol. 327, The Initial Mass Function: from Salpeter 1955 to 2005. Springer, Dordrecht, p. 41

Chen Y., Girardi L., Bressan A., Marigo P., Barbieri M., Kong X., 2014, MNRAS, 444, 2525

Cieza L. A., Kessler-Silacci J. E., Jaffe D. T., Harvey P. M., Evans N. J., II, 2005, ApJ, 635, 422

Comerón F., 2011, A&A, 531, A33

Correia S., Zinnecker H., Ratzka T., Sterzik M. F., 2006, A&A, 459, 909

Czekaj M. A., Robin A. C., Figueras F., Luri X., Haywood M., 2014, A&A, 564, A102

D'Antona F., Mazzitelli I., 1997, Mem. Soc. Astron. Ital., 68, 807

Da Rio N., Robberto M., Hillenbrand L. A., Henning T., Stassun K. G., 2012, ApJ, 748, 14

Daemgen S., Petr-Gotzens M. G., Correia S., Teixeira P. S., Brandner W., Kley W., Zinnecker H., 2013, A&A, 554, A43

Dawson P., Scholz A., Ray T. P., Marsh K. A., Wood K., Natta A., Padgett D., Ressler M. E., 2013, MNRAS, 429, 903

De Marchi G., Paresce F., Zwart S. P., 2005, in Corbelli E., Palla F., Zinnecker H., eds, Astrophysics and Space Science Library, Vol. 327, The Initial Mass Function 50 Years Later. Springer, Dordrecht, p. 77

DeRose K. L., Bourke T. L., Gutermuth R. A., Wolk S. J., Megeath S. T., Alves J., Nürnberger D., 2009, AJ, 138, 33

Devillard N., 1997, The Messenger, 87, 19

Diolaiti E., Bendinelli O., Bonaccini D., Close L., Currie D., Parmeggiani G., 2000, A&AS, 147, 335

Downes J. J., Briceño C., Hernández J., Calvet N., Hartmann L., Ponsot Balaguer E., 2008, AJ, 136, 51

Drass H., Haas M., Chini R., Bayo A., Hackstein M., Hoffmeister V., Godoy N., Vogt N., 2016, MNRAS, 461, 1734

Duchêne G., Kraus A., 2013, ARA&A, 51, 269

Fukui Y. et al., 2016, ApJ, 820, 26

Getman K. V. et al., 2014, ApJ, 787, 108

Grellmann R., Preibisch T., Ratzka T., Kraus S., Helminiak K. G., Zinnecker H., 2013, A&A, 550, A82

Gutermuth R. A., Megeath S. T., Pipher J. L., Williams J. P., Allen L. E., Myers P. C., Raines S. N., 2005, ApJ, 632, 397

Gutermuth R. A., Megeath S. T., Myers P. C., Allen L. E., Pipher J. L., Fazio G. G., 2009, ApJS, 184, 18

Habibi M., Stolte A., Brandner W., Hußmann B., Motohara K., 2013, A&A, 556, A26

Harayama Y., Eisenhauer F., Martins F., 2008, ApJ, 675, 1319

Hennebelle P., Chabrier G., 2009, ApJ, 702, 1428

Hernández J., Calvet N., Hartmann L., Briceño C., Sicilia-Aguilar A., Berlind P., 2005, AJ, 129, 856

Hußmann B., Stolte A., Brandner W., Gennaro M., Liermann A., 2012, A&A, 540, A57

King R. R., Parker R. J., Patience J., Goodwin S. P., 2012a, MNRAS, 421, 2025

King R. R., Goodwin S. P., Parker R. J., Patience J., 2012b, MNRAS, 427, 2636

Köhler R., Petr-Gotzens M. G., McCaughrean M. J., Bouvier J., Duchêne G., Quirrenbach A., Zinnecker H., 2006, A&A, 458, 461

Kounkel M., Hartmann L., Tobin J. J., Mateo M., Bailey J. I., III, Spencer M., 2016a, ApJ, 821, 8

Kounkel M., Megeath S. T., Poteet C. A., Fischer W. J., Hartmann L., 2016b, ApJ, 821, 52

Kroupa P., 2001, MNRAS, 322, 231

Kuhn M. A. et al., 2014, ApJ, 787, 107

Kuhn M. A., Getman K. V., Feigelson E. D., 2015a, ApJ, 802, 60

Kuhn M. A., Feigelson E. D., Getman K. V., Sills A., Bate M. R., Borissova J., 2015b, ApJ, 812, 131

Kuiper G. P., 1935, PASP, 47, 121

Lenzen R. et al., 2003, in Iye M., Moorwood A. F. M., eds, Proc. SPIE, Vol. 4841, Instrument Design and Performance for Optical/Infrared Ground-based Telescopes. SPIE, Bellingham, p. 944

Licquia T. C., Newman J. A., 2015, ApJ, 806, 96

Lodieu N., 2013, MNRAS, 431, 3222

Lucas P. W., Roche P. F., Tamura M., 2005, MNRAS, 361, 211

Luhman K. L., 2004a, ApJ, 602, 816

Luhman K. L., 2004b, ApJ, 617, 1216

Luhman K. L., 2007, ApJS, 173, 104

Luhman K. L., 2012, ARA&A, 50, 65

Luhman K. L., Muench A. A., 2008, ApJ, 684, 654

Luhman K. L., Esplin T. L., Loutrel N. P., 2016, ApJ, 827, 52

Marks M., Kroupa P., 2012, A&A, 543, A8

Meyer M. R., Calvet N., Hillenbrand L. A., 1997, AJ, 114, 288

Moorwood A. et al., 1998, The Messenger, 94, 7

Morrell N., Levato H., 1991, ApJS, 75, 965

Muench A. A., Lada E. A., Lada C. J., Alves J., 2002, ApJ, 573, 366

Murphy D. C., 1985, PhD thesis, Massachusetts Institute of Technology, Cambridge, MA

Muzzio J. C., 1979, AJ, 84, 639

Mužić K., Scholz A., Geers V. C., Jayawardhana R., López Martí B., 2014, ApJ, 785, 159

Mužić K., Scholz A., Geers V. C., Jayawardhana R., 2015, ApJ, 810, 159

Padoan P., Nordlund Å., 2002, ApJ, 576, 870

Pecaut M. J., Mamajek E. E., 2013, ApJS, 208, 9

Peña Ramírez K., Béjar V. J. S., Zapatero Osorio M. R., Petr-Gotzens M. G., Martín E. L., 2012, ApJ, 754, 30

Pettersson B., 2008, in Reipurth B., ed., ASP Monograph Publications, Handbook of Star Forming Regions, Vol. II: The Southern Sky. Astron. Soc. Pac., San Francisco, p. 43

Reipurth B., Guimarães M. M., Connelley M. S., Bally J., 2007, AJ, 134, 2272

Robin A. C., Reylé C., Derrière S., Picaud S., 2003, A&A, 409, 523

Rochau B. et al., 2011, MNRAS, 418, 949

Rousset G. et al., 2003, in Wizinowich P. L., Bonaccini D., eds, Proc. SPIE, Vol. 4839, Adaptive Optical System Technologies II. SPIE, Bellingham, p. 140

Salpeter E. E., 1955, ApJ, 121, 161

Schödel R., 2010, A&A, 509, A58

Scholz A., Muzic K., Geers V., Bonavita M., Jayawardhana R., Tamura M., 2012a, ApJ, 744, 6

Scholz A., Jayawardhana R., Muzic K., Geers V., Tamura M., Tanaka I., 2012b, ApJ, 756, 24

Scholz A., Geers V., Clark P., Jayawardhana R., Muzic K., 2013, ApJ, 775, 138

Siess L., Dufour E., Forestini M., 2000, A&A, 358, 593

Skrutskie M. F. et al., 2006, AJ, 131, 1163

Slesnick C. L., Hillenbrand L. A., Carpenter J. M., 2004, ApJ, 610, 1045

Snaith O., Haywood M., Di Matteo P., Lehnert M. D., Combes F., Katz D., Gómez A., 2015, A&A, 578, A87

Stolte A., Brandner W., Brandl B., Zinnecker H., 2006, AJ, 132, 253

Weights D. J., Lucas P. W., Roche P. F., Pinfield D. J., Riddick F., 2009, MNRAS, 392, 817

Whitworth A. P., Zinnecker H., 2004, A&A, 427, 299

Winston E., Wolk S. J., Bourke T. L., Megeath S. T., Gutermuth R., Spitzbart B., 2011, ApJ, 743, 166

Wolk S. J., Spitzbart B. D., Bourke T. L., Alves J., 2006, AJ, 132, 1100

Wolk S. J., Bourke T. L., Vigil M., 2008, in Reipurth B., ed., ASP Monograph Publications, Handbook of Star Forming Regions, Vol. II: The Southern Sky. Astron. Soc. Pac., San Francisco, p. 124

Yamaguchi N., Mizuno N., Saito H., Matsunaga K., Mizuno A., Ogawa H., Fukui Y., 1999, PASJ, 51, 775

Zinnecker H., McCaughrean M., 1991, Mem. Soc. Astron. Ital., 62, 761

This paper has been typeset from a TEX/LATEX file prepared by the author.